forests

MDPI

Article

Evaluating the Marginal Contribution of Remote Sensing for Forest Biomass Estimation When Inventory Data Exists

Xiaoman Zheng [1,2,3,†], Ying Su [4,†], Yunxia Wang [5], Shaoqing Dai [6], Yufeng Chi [1], Guanjun Lin [1] and Yin Ren [2,3,7,*]

1 Fujian Key Lab of Agriculture IOT Application, School of Information Engineering, Sanming University, Sanming 365004, China; xmzheng@fjsmu.edu.cn (X.Z.)
2 Key Laboratory of Urban Environment and Health, Institute of Urban Environment, Chinese Academy of Sciences, Xiamen 361021, China
3 Fujian Key Laboratory of Watershed Ecology, Institute of Urban Environment, Chinese Academy of Sciences, Xiamen 361021, China
4 State Key Laboratory of Marine Environmental Science, College of Ocean and Earth Sciences, Xiamen University, Xiamen 361102, China
5 Royal Botanic Garden Edinburgh, Edinburgh EH3 5LR, UK
6 School of Resource and Environmental Sciences, Wuhan University, Wuhan 430072, China
7 Ningbo Urban Environment Observation and Research Station—NUEORS, Chinese Academy of Sciences, Ningbo 315800, China
* Correspondence: yren@iue.ac.cn
† These authors contributed equally to this work.

Abstract

Combining remote sensing data with field inventory data is a common practice in estimation of forest Aboveground Biomass (AGB). However, in areas with well-established ground monitoring systems, the actual added value of this combination has not been fully quantified. This paper aims to critically assess the marginal contribution of optical remote sensing data to AGB estimation when the forest inventory data are already available, and further investigates error sources and residual distributions. Using Longyan City, Fujian Province as a case study, we systematically tested the effects of data types (inventory only, Landsat 8 only, inventory + Landsat 8, and inventory + Landsat 8 + meteorological data), sampling methods, and statistical models on plot-scale AGB estimation accuracy, along with uncertainty distribution across biomass levels. Inventory data alone (stand age and canopy cover) achieved acceptable accuracy, with R^2 = 0.60 and RMSE = 35.78 t/ha under the optimal configuration (RandomForest + ShuffleSplit_5). Adding Landsat 8 data yielded only modest improvements: RMSE decreased by 5.3% and R^2 increased by 6.7% relative to the inventory-only baseline. When the optimal combination for each data type was evaluated on the independent test set, the highest R^2 reached only 0.56, leaving approximately 44% of the observed variation in plot-level AGB unexplained. ANOVA showed that data type was the dominant factor, accounting for 73.0% of the variation in RMSE, followed by model choice (15.1%) and their interaction (8.5%), whereas the contribution of the validation scheme was less than 3.0%. We further examined residual distributions across biomass levels and found that residual skewness shifted systematically: negative skewness (overestimation) prevailed in low-biomass plots, near-zero skewness in medium-biomass plots, and positive skewness (underestimation) in high-biomass plots. Among all data types, the Landsat-only configuration exhibited the most severe bias at both low and high biomass extremes; adding remote sensing and climate data to inventory data did not substantially correct this bias structure. Overall, these findings demonstrate that in regions with high-quality ground inventory, the marginal gains from integrating optical remote sensing are limited—both in terms of overall accuracy and the structure of prediction

Academic Editor: Michael Sprintsin

Received: 6 August 2026
Revised: 3 September 2026
Accepted: 10 September 2026
Published: 14 September 2026

errors. The unexplained variance and systematic residual biases across biomass gradients highlight the need for better representation of high-biomass stands and suggest that future efforts should prioritize sample augmentation in under-represented biomass classes, rather than relying solely on multisource data fusion for accuracy improvement.

Keywords: marginal contribution; data fusion; forest biomass estimation; forest inventory data; optical remote sensing

1. Introduction

The precise estimation of forest Aboveground Biomass (AGB) is crucial for quantifying carbon stocks, giving details about climate change mitigation strategies such as REDD+ and supporting sustainable forest management [1]. To achieve this goal, the combination of multisource data, especially the combination of forest inventory data and satellite remote sensing data, has become one mainstream paradigm of Forest Science [2–5]. This paradigm is founded on the realization that the inventory data are accurate at the plot scale, coverage is limited and it is expensive to cover large areas, whereas remote sensing offers spatial and temporal continuity of wall-to-wall coverage [3,6,7].

Optical remote sensing data (e.g., from Landsat) provide spectral indices and related environmental information for regional-scale AGB mapping [8,9]. Recent reviews have highlighted the increasing use of optical, SAR, and LiDAR data, as well as their integration, for forest AGB estimation, while also emphasizing that estimation accuracy depends strongly on sensor characteristics, forest structure, spatial scale, and modeling methods [10,11]. Recent studies have demonstrated the potential of high-resolution PlanetScope imagery to capture fine-scale spatial heterogeneity and support AGB estimation and mapping in coastal, palustrine, and tidal wetlands [12–14]. Although wetland vegetation differs structurally from forests, these studies provide useful context for understanding the potential value of finer-resolution optical imagery in biomass estimation. However, optical remote sensing is fundamentally constrained by the indirect and saturable relationship between spectral reflectance and forest structural attributes such as biomass [15,16]. Large-scale carbon-balance estimates derived from optical data have also been questioned because of accuracy limitations and the potential to overstate current mapping capabilities [17,18]. In contrast, well-designed forest inventory data remain the accuracy benchmark for local-scale AGB estimation [19–21]. This background provides a clear rationale for data fusion by combining the spatial scalability of remote sensing with the accuracy of ground measurements. Many studies have demonstrated that this integration can improve estimation accuracy [4,5].

However, a key and often neglected problem concerns areas where high-quality and systematic forest inventory data already exist—how much marginal gain can the integration of optical remote sensing data bring? Under these conditions, the automatic assumption that "fusion always produces significantly better estimates" may not hold, but may lead to potential redundant complexity in the monitoring frameworks. The conceptual trade-offs between the two data sources are illustrated in Figure 1. While the synergy between them motivates data fusion, the extent to which remote sensing can add value to existing high-quality inventory systems remains an open question.

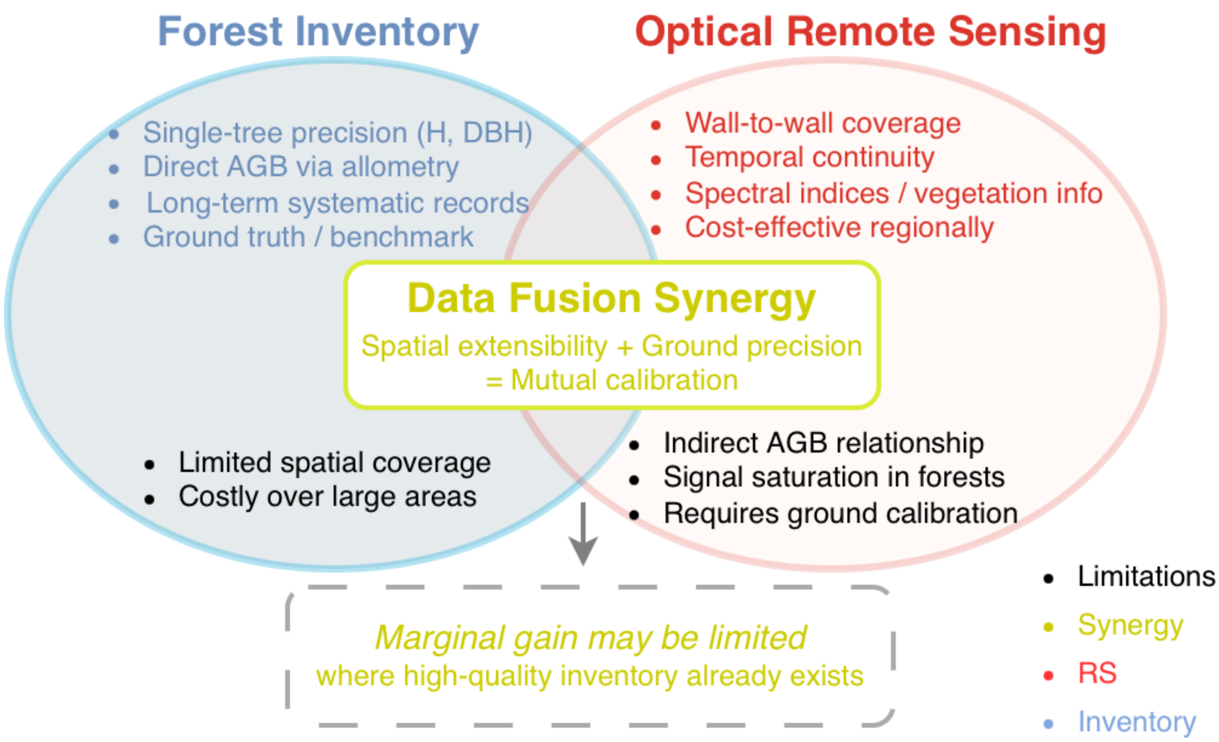

Figure 1. Conceptual Venn diagram illustrating the respective strengths, limitations, and synergies of forest inventory data and optical remote sensing data for AGB estimation. H = tree height, DBH = tree diameter at breast height, RS = remote sensing.

Here, we addressed this issue through a rigorous and controlled benchmark study conducted in Longyan City, Fujian Province, a subtropical forest region with a well-established inventory system. This study aimed to evaluate the marginal contribution of optical remote sensing data to plot-scale AGB estimation when high-quality forest inventory data were already available. In this study, the marginal contribution of remote sensing refers to the incremental improvement in AGB estimation accuracy achieved by adding remote sensing variables to inventory-based predictors. To operationalize this aim, three research questions (RQs) and their corresponding hypotheses were posed: RQ1: When high-quality inventory predictors (stand age and canopy cover) are already available at the plot scale, how much marginal improvement in AGB estimation accuracy can the addition of optical remote sensing and meteorological data provide? H1: The marginal improvement would be limited and statistically insignificant in most model configurations. RQ2: What are the relative contributions of data type, statistical model, and cross-validation design to the variation in estimation accuracy? H2: Data type would dominate the variation in accuracy, far exceeding the effects of model and validation design. RQ3: How are prediction errors distributed across biomass strata and data combinations, and which combinations or biomass levels are most prone to large errors? H3: Prediction errors would be largest in high-biomass strata and under Landsat-only configurations.

2. Materials and Methods

To provide a clear overview of the analytical framework, Figure 2 presents the complete technical flowchart of this study.

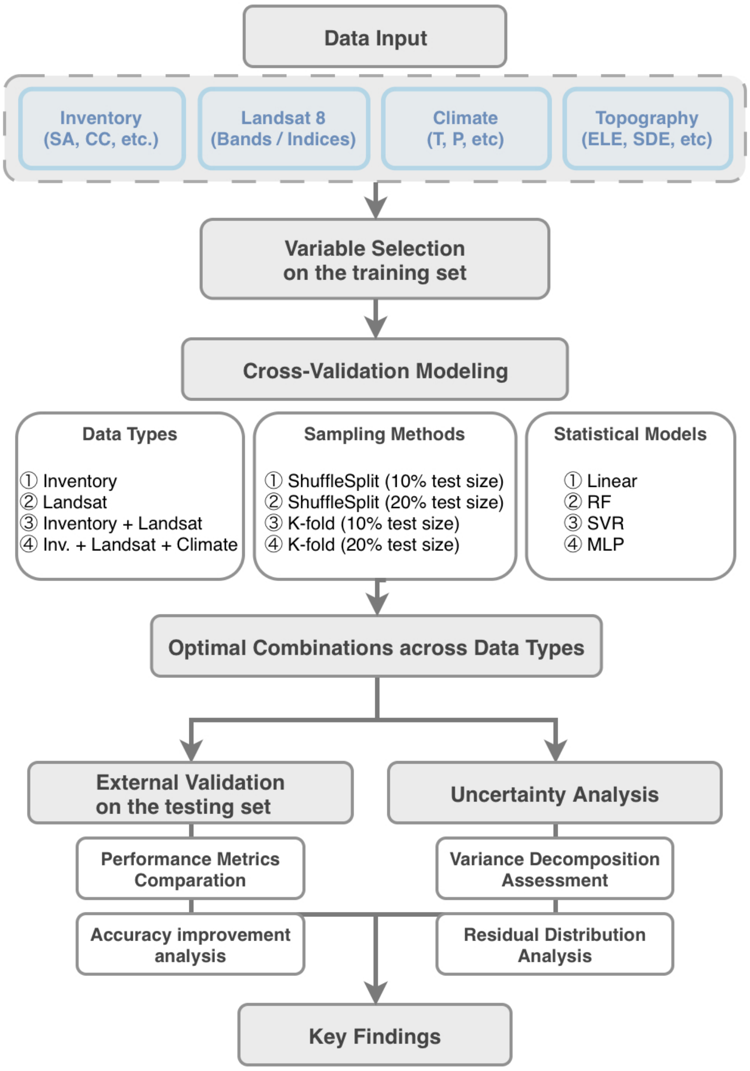

Figure 2. Workflow of the study. SA = stand age, CC = canopy cover, T = temperature, P = precipitation, ELE = elevation, SDE = soil depth, SVR= Support Vector Regression, RF = Random Forest, MLP = Multi-Layer Perceptron.

2.1. Study Area

We conducted our study in the mountainous subtropical forest region of Longyan City, located in Fujian Province, Southeastern China (Figure 3). Fujian Province has the highest forest cover in China, and within Fujian, Longyan City has the highest forest cover, accounting for approximately 78% of its land area. The climate in Fujian is characterized by a subtropical monsoon climate, with an average annual rainfall of around 1700 mm and mean annual temperatures ranging from 17 to 21 °C.

The study area spans approximately 19,000 km^2 and is situated at 24°23′ to 26°02′ N latitude and 115°51′ to 117°45′ E longitude. Longyan City exhibits significant variations in elevation, ranging from 69 to 1811 m, resulting in complex topography. The region also displays substantial spatiotemporal heterogeneity in forest composition, structure, and biomass. The dominant tree species in the study area include *Pinus massoniana* Lamb., *Cunninghamia lanceolata* (Lamb.) Hook., and species belonging to the families Fagaceae and Lauraceae. For this study, we used 590 permanent sample plots established by the Forest Resource Inventory of China (FRIC) in Longyan City (Figure 3). The FRIC adopted a stratified multi-stage systematic sampling design, with sample plots distributed on a regular grid at an interval of approximately 4 km × 6 km. This sampling design ensures a relatively uniform spatial distribution of plots and provides broad coverage of the major topographic conditions, forest types, and stand structures within the study area, thereby enhancing the spatial representativeness of the inventory data. Each permanent sample plot covers an area of 666.67 m^2 (25.82 m × 25.82 m) and was permanently marked for periodic remeasurement.

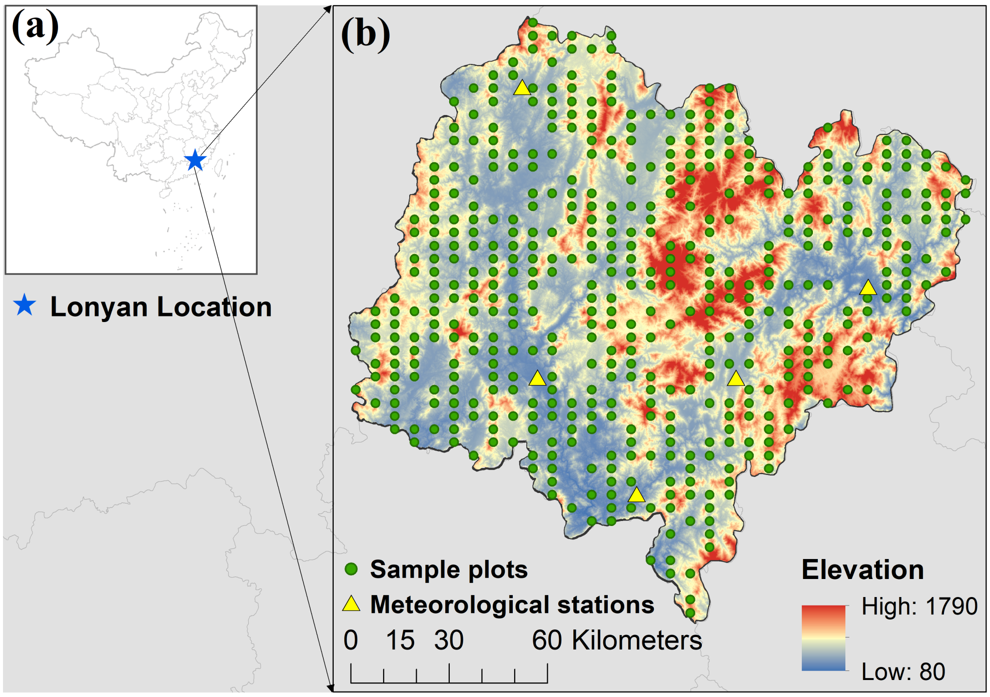

Figure 3. Study area in Longyan City, Fujian Province, China. (**a**) Location of Longyan City in China; (**b**) Distribution of sample plots and meteorological stations in Longyan City.

2.2. Data Preparation

The dataset employed in this paper comprised observations of forest AGB as well as predictor variables. The predictor variables encompassed a range of data sources, including forest inventory data obtained from field research, remote sensing data (specifically Landsat 8 data and Advanced Land Observing Satellite (ALOS) data), and meteorological data.

2.2.1. AGB Reference Data

This dataset contained the reference AGBs of all 590 plots within the study area. The AGB of each plot was determined by summing the AGBs of all trees present within that plot (Table 1). To estimate the AGB of each tree, several variables were considered, including tree height (*H*, m), tree diameter at breast height (*DBH*, cm), tree species, and 9 allometric models previously established by the research team [22]. The details of these 9 single tree models are provided in Table A1. These allometric models differed in their applicable scope: some were developed for specific tree species, some for a family or group of species, and others for mixed species. For each tree within a plot, the most appropriate equation was selected according to its species and the applicable scope of the models listed in Table A1. The plot-level AGB density (t/ha) was then obtained by summing the AGB estimates of all trees in the plot and dividing by the plot area.

Table 1. Statistical information of full tree surveys.

Number of Trees	Number of Species	DBH (cm)	H (m)
50,579	207	5.0–134.6 (10.80)	0.8–21.8 (9.88)

Values are presented as minimum–maximum (mean).

2.2.2. Forest Inventory Data

Forest inventory data for a total of 590 plots were meticulously observed, measured, and recorded in the field by China's FRIC using its sampling survey technology for forest resources monitoring system. The inventory was conducted in 2013 as part of the eighth National Forest Inventory of Fujian Province. Tree-level measurements included tree species, *DBH*, and representative *H*. Stand origin and species composition were also recorded, allowing the plots to be characterized as natural or planted forests and as pure or mixed stands. The collected data encompassed various aspects, including: (1) forest-related information such as vegetation type, dominant species, stand age, and canopy cover; (2) soil characteristics such as soil depth, soil type, humus depth, and forest litter depth; and (3) topographical features such as elevation, slope, aspect, and position. For detailed statistical information regarding the 590 sample plots, please refer to Table 2.

Table 2. Statistical information of 590 sample plots.

Items	Values	Items	Values
Vegetation types	11 types	Elevation (m) [a]	189∼1690 (621.0)
Slope position	6 types	Degree of slope (°) [a]	0∼60 (27.3)
Slope direction	9 types	Stand age (year) [a]	2∼65 (25.7)
Dominant species types	16	Canopy cover (%) [a]	20∼90 (62.0)
Soil types	4 types	Soil depth (cm) [a]	20∼180 (89.1)
Humus layer thickness (cm) [a]	1∼40 (9.6)	Forest litter depth (cm) [a]	0∼50 (4.9)
Landform types	5 types		

[a] provides minimum–maximum (mean) values. Vegetation type, dominant species type, slope position, slope direction, soil type, and landform type are categorical attributes recorded in the FRIC field survey; the values indicate the number of categories observed for each attribute.

2.2.3. Landsat 8 Surface Reflectance

All available Landsat 8 Operational Land Imager (OLI) surface reflectance images acquired between 1 June and 31 October 2013 were obtained from the Google Earth Engine (GEE) platform. This period corresponded to the year of the forest inventory and covered the main growing season in Longyan, during which the subtropical forest canopy was fully developed and relatively stable. Therefore, the selected images were considered representative of the forest canopy conditions during the inventory period.

Before compositing, pixels affected by clouds, cirrus, and cloud shadows were masked using the quality-assurance (QA) band provided with the Landsat 8 surface reflectance product. NDVI was subsequently calculated for each valid observation, and a pixel-wise maximum-NDVI composite was generated. This compositing strategy retained the observation with the strongest vegetation signal for each pixel and helped reduce the effects of residual cloud and haze contamination and short-term phenological variation. The spectral and texture variables used in the subsequent analyses were derived from this composite image at a spatial resolution of 30 m. The spectral ranges of the Landsat 8 bands used in this study are summarized in Table 3.

(a) Vegetation index

We computed three vegetation indices for the study area at a 30 m resolution: NDVI (Equation (1)), the Improved NDVI value specific to the study area ($NDVI_C$, Equation (2)), and the Soil Adjusted Vegetation Index (SAVI, Equation (3)). These indices are extensively employed in predicting forest biomass and other forest structures [23]. We also calculated three Normalized Difference Water Index (NDWI) variants: NDWI, $NDWI_{1640}$, and $NDWI_{2130}$. NDWI was calculated using the green and near-infrared bands, whereas

$NDWI_{1640}$ and $NDWI_{2130}$ were calculated using the near-infrared band and the short-wave infrared bands centered near 1640 and 2130 nm, respectively (Equations (4)–(6)).

$$\mathrm{NDVI} = \frac{(\mathrm{NIR} - \mathrm{R})}{(\mathrm{NIR} + \mathrm{R})} \tag{1}$$

$$\mathrm{NDVI_C} = \mathrm{NDVI} \times \left[1 - \frac{\mathrm{MIR} - \mathrm{MIR_{min}}}{\mathrm{MIR_{max}} - \mathrm{MIR_{min}}}\right] \tag{2}$$

$$\mathrm{SAVI} = \left[\frac{(\mathrm{NIR} - \mathrm{R})}{(\mathrm{NIR} + \mathrm{R}) + \mathrm{L}}\right](1 + \mathrm{L}) \tag{3}$$

$$\mathrm{NDWI} = \frac{\mathrm{G} - \mathrm{NIR}}{\mathrm{G} + \mathrm{NIR}} \tag{4}$$

$$\mathrm{NDWI_{1640}} = \frac{\mathrm{NIR} - \mathrm{MIR_{1640}}}{\mathrm{NIR} + \mathrm{MIR_{1640}}} \tag{5}$$

$$\mathrm{NDWI_{2130}} = \frac{\mathrm{NIR} - \mathrm{MIR_{2130}}}{\mathrm{NIR} + \mathrm{MIR_{2130}}} \tag{6}$$

where G is the green band; NIR is the near-infrared band; R is the red band; MIR is the short-wave infrared band; MIR_{1640} and MIR_{2130} are the short-wave infrared bands centered near 1640 and 2130 nm, respectively; MIR_{max} and MIR_{min} are the short-wave infrared band values of the closed and open canopies, and the highest and the lowest values extracted from the short-wave infrared bands within the forest area are taken as the values of MIR_{max} and MIR_{min} [24]; L is the soil brightness correction coefficient, which takes the value of 0.5 [25].

Table 3. Band description.

Name	Description	Units	Wavelength
B2	Band 2 (blue) surface reflectance	/	0.452∼0.512 µm
B3	Band 3 (green) surface reflectance	/	0.533∼0.590 µm
B4	Band 4 (red) surface reflectance	/	0.636∼0.673 µm
B5	Band 5 (near infrared) surface reflectance	/	0.851∼0.879 µm
B6	Band 6 (shortwave infrared 1) surface reflectance	/	1.566∼1.651 µm
B7	Band 7 (shortwave infrared 2) surface reflectance	/	2.107∼2.294 µm
B10	Band 10 brightness temperature. This band, while originally collected with a resolution of 100 m/pixel, has been resampled using cubic convolution to 30 m.	Celsius	10.60∼11.19 µm
B11	Band 11 brightness temperature. This band, while originally collected with a resolution of 100 m/pixel, has been resampled using cubic convolution to 30 m.	Celsius	11.50∼12.51 µm

(b) Texture information for bands 2∼7

Texture feature variables were computed for bands 2–7, encompassing mean, variance, contrast, correlation, dissimilarity, angular second moment, inverse difference moment, entropy, and sum average [26]. The three window sizes were selected to capture texture information related to AGB at different spatial scales because the relationship between forest AGB and texture features may vary with window size [27,28]. These computations were performed within pixel windows of sizes 3 × 3, 5 × 5, and 7 × 7, resulting in a total of 162 texture feature variables (Table 4).

Among these variables, the mean represents the average value of the measured gray level, while variance measures how spread out the distribution of gray levels is. Contrast measures the local contrast of an image, while correlation measures the correlation between pairs of pixels. Dissimilarity captures the dissimilarity between pairs of measured pixels. The angular second moment measures the number of repeated pairs, and the inverse difference moment assesses homogeneity. Entropy characterizes the randomness in the distribution of the measured gray level, and the total mean represents the overall average value of the measured gray level.

Table 4. Texture information for bands 2∼7.

Texture Information	Bands					
	2	3	4	5	6	7
Mean (MEA)	px3_B2_mea px5_B2_mea px7_B2_mea	px3_B3_mea px5_B3_mea px7_B3_mea	px3_B4_mea px5_B4_mea px7_B4_mea	px3_B5_mea px5_B5_mea px7_B5_mea	px3_B6_mea px5_B6_mea px7_B6_mea	px3_B7_mea px5_B7_mea px7_B7_mea
Variance (VAR)	px3_B2_var px5_B2_var px7_B2_var	px3_B3_var px5_B3_var px7_B3_var	px3_B4_var px5_B4_var px7_B4_var	px3_B5_var px5_B5_var px7_B5_var	px3_B6_var px5_B6_var px7_B6_var	px3_B7_var px5_B7_var px7_B7_var
Contrast (CON)	px3_B2_con px5_B2_con px7_B2_con	px3_B3_con px5_B3_con px7_B3_con	px3_B4_con px5_B4_con px7_B4_con	px3_B5_con px5_B5_con px7_B5_con	px3_B6_con px5_B6_con px7_B6_con	px3_B7_con px5_B7_con px7_B7_con
Correlation (COR)	px3_B2_cor px5_B2_cor px7_B2_cor	px3_B3_cor px5_B3_cor px7_B3_cor	px3_B4_cor px5_B4_cor px7_B4_cor	px3_B5_cor px5_B5_cor px7_B5_cor	px3_B6_cor px5_B6_cor px7_B6_cor	px3_B7_cor px5_B7_cor px7_B7_cor
Dissimilarity (DIS)	px3_B2_dis px5_B2_dis px7_B2_dis	px3_B3_dis px5_B3_dis px7_B3_dis	px3_B4_dis px5_B4_dis px7_B4_dis	px3_B5_dis px5_B5_dis px7_B5_dis	px3_B6_dis px5_B6_dis px7_B6_dis	px3_B7_dis px5_B7_dis px7_B7_dis
Angular second moment (ASM)	px3_B2_asm px5_B2_asm px7_B2_asm	px3_B3_asm px5_B3_asm px7_B3_asm	px3_B4_asm px5_B4_asm px7_B4_asm	px3_B5_asm px5_B5_asm px7_B5_asm	px3_B6_asm px5_B6_asm px7_B6_asm	px3_B7_asm px5_B7_asm px7_B7_asm
Inverse differential moment (IDM)	px3_B2_idm px5_B2_idm px7_B2_idm	px3_B3_idm px5_B3_idm px7_B3_idm	px3_B4_idm px5_B4_idm px7_B4_idm	px3_B5_idm px5_B5_idm px7_B5_idm	px3_B6_idm px5_B6_idm px7_B6_idm	px3_B7_idm px5_B7_idm px7_B7_idm
Entropy (ENT)	px3_B2_ent px5_B2_ent px7_B2_ent	px3_B3_ent px5_B3_ent px7_B3_ent	px3_B4_ent px5_B4_ent px7_B4_ent	px3_B5_ent px5_B5_ent px7_B5_ent	px3_B6_ent px5_B6_ent px7_B6_ent	px3_B7_ent px5_B7_ent px7_B7_ent
Sum of average value (SAV)	px3_B2_sav px5_B2_sav px7_B2_sav	px3_B3_sav px5_B3_sav px7_B3_sav	px3_B4_sav px5_B4_sav px7_B4_sav	px3_B5_sav px5_B5_sav px7_B5_sav	px3_B6_sav px5_B6_sav px7_B6_sav	px3_B7_sav px5_B7_sav px7_B7_sav

Note: px3 indicates a 3 × 3 pixel window, px5 indicates a 5 × 5 pixel window, and px7 indicates a 7 × 7 pixel window.

2.2.4. Topographic Data

The ALOS Global Digital Surface Model (AW3D30) dataset provides detailed information with a horizontal resolution of approximately 30 m (1 arcsec mesh) [29]. From this dataset, we extracted four essential topographic variables: elevation (ALOS_DSM, measured in meters), slope (DSM_slope, measured in degrees), slope direction (DSM_aspect, measured in degrees), and hillshade (DSM_hillshade, unitless). These variables were used to characterize the terrain conditions of the study area.

2.2.5. Meteorological Data

Meteorological data for the study were sourced from the monitoring data of meteorological stations in Fujian Province for the year 2013. The mean values of the meteorological elements at each station in 2013 were extracted, combined with the ALOS DEM data, and spatially interpolated by applying the Anusplin software [30]. The interpolated meteorological variables were then extracted individually at each of the 590 plot locations. Table 5 summarizes the distribution of these plot-level values, including the mean, standard deviation, minimum, maximum, and median.

Table 5. Average value of meteorological elements of sample plots in 2013.

Meteorological Element	Air Pressure (hPa)	Relative Humidity (%)	Mean Temperatures (°C)	Maximum Temperature (°C)	Minimum Temperature (°C)	Mean 2-min Wind Speed (m/s)	Maximum Wind Speed (m/s)	Daily Precipitation (mm)
Mean	944.91	71.62	19.09	30.57	8.93	9.94	1.59	216.00
Standard deviation	27.69	4.05	0.80	0.88	0.92	2.13	0.17	54.30
Minimum value	831.40	60.87	15.89	27.03	5.73	6.52	1.22	108.44
Maximum value	993.44	79.99	20.86	32.63	10.67	18.18	1.91	416.44
Median	949.44	71.73	19.17	30.68	9.02	9.61	1.59	208.12

2.3. Modeling and Evaluation Framework

2.3.1. Data Splitting

To objectively evaluate the generalization ability of the models, the entire dataset was randomly split into an internal training set (80%) and an independent test set (20%) with a fixed random seed ($random\_state = 42$) to ensure reproducibility. The internal training set was used for variable selection, model training, and cross-validation, while the independent test set was kept completely unseen throughout the model development process and used only once to evaluate the final selected models.

2.3.2. Variable Selection on the Training Set

Variable selection was performed exclusively on the internal training set. Pearson correlation coefficients were calculated between each candidate variable and the reference AGB, and variables with $|r| \geq 0.30$ were retained for subsequent modeling. Two-sided significance tests were also conducted, and the corresponding p-values were reported to characterize the statistical significance of the correlations. To avoid circularity, H and DBH were excluded from the correlation analysis and subsequent modeling.

2.3.3. Cross-Validation Experimental Design

A three-factor full factorial design was adopted on the internal training set to systematically evaluate the effects of data type, cross-validation method, and statistical model on AGB estimation accuracy. The three factors were: (1) data type (4 levels): Inventory, Landsat, Inv_Landsat, and Inv_Landsat_Climate; (2) cross-validation method (4 levels): 5-fold KFold, 10-fold KFold, 5-repetition ShuffleSplit, and 10-repetition ShuffleSplit; (3) statistical model (4 levels): Linear Regression, Random Forest (RF), Support Vector Regression (SVR), and Multi-Layer Perceptron (MLP). This yielded a total of $4 \times 4 \times 4 = 64$ experimental combinations.

Two families of cross-validation schemes were employed. In k-fold cross-validation (KFold), the internal training set was randomly partitioned into k mutually exclusive folds of approximately equal size; each fold served once as the validation set, while the remaining $k - 1$ folds were used to fit the model, and the k validation results were averaged. In contrast, ShuffleSplit (repeated random subsampling validation) repeatedly generated independent random splits of the data into training and validation subsets with a fixed ratio (80%/20% here); unlike KFold, the validation subsets in different repetitions may overlap, and the proportion of the data used for validation is not tied to the number of repetitions. For ShuffleSplit with 5 or 10 repetitions, the validation results of all repetitions were averaged. Both schemes were implemented using the KFold and ShuffleSplit functions in scikit-learn [31].

To ensure fair model comparison, hyperparameter optimization was performed for RF, SVR, and MLP separately for each data type using 5-fold grid search on the internal training set. For RF, the search covered n_estimators (50, 100), max_depth (10, 20, None), min_samples_split (2, 5), and min_samples_leaf (1, 2); for SVR, the search covered C (0.5, 1.0, 2.0), gamma ('scale', 0.1, 0.5), and epsilon (0.05, 0.10, 0.15); for MLP, the search covered hidden_layer_sizes ((50,), (100,)), alpha (0.001, 0.01), and learning_rate_init (0.001, 0.01), with solver fixed to 'adam' and activation to 'relu'. The optimized hyperparameters are summarized in Table 6. Linear Regression used default settings.

Table 6. Optimized hyperparameters of RF, SVR, and MLP for different data types.

Data Type	RF	SVR	MLP

Inventory	max_depth = None;
	min_samples_leaf = 2;
	min_samples_split = 5;
	n_estimators = 100
		C = 2.0;
		epsilon = 0.05;
		gamma = scale
			activation = relu;
			alpha = 0.001;
			hidden_layer_sizes = (100,);
			learning_rate_init = 0.01;
			solver = adam

Landsat	max_depth = 10;
	min_samples_leaf = 1;
	min_samples_split = 2;
	n_estimators = 100
		C = 2.0;
		epsilon = 0.05;
		gamma = scale
			activation = relu;
			alpha = 0.001;
			hidden_layer_sizes = (100,);
			learning_rate_init = 0.001;
			solver = adam

Inv_Landsat	max_depth = None;
	min_samples_leaf = 2;
	min_samples_split = 2;
	n_estimators = 50
		C = 2.0;
		epsilon = 0.15;
		gamma = scale
			activation = relu;
			alpha = 0.01;
			hidden_layer_sizes = (50,);
			learning_rate_init = 0.01;
			solver = adam

Inv_Landsat_
Climate
	max_depth = 20;
	min_samples_leaf = 2;
	min_samples_split = 2;
	n_estimators = 100
		C = 2.0;
		epsilon = 0.10;
		gamma = scale
			activation = relu;
			alpha = 0.01;
			hidden_layer_sizes = (100,);
			learning_rate_init = 0.01;
			solver = adam

2.3.4. Performance Metrics and Identification of Optimal Combination

Cross-validation was used, and model performance was evaluated using the validation set from each fold or random split. For each combination, four evaluation metrics were calculated: Mean Absolute Error (MAE, Equation (7)), Mean Relative Error (MRE, Equation (8)), Root Mean Square Error (RMSE, Equation (9)), and Coefficient of Determination (R^2, Equation (10)). For KFold methods, the metrics from each fold were recorded and summarized as mean and standard deviation across folds. For ShuffleSplit methods, the same procedure was applied to each random partition. The formulas for these metrics are as follows:

$$\mathrm{MAE} = \left(\sum_{i=1}^{n} \left| y_i^p - y_i \right| \right) / n \quad (7)$$

$$\mathrm{MRE} = \left(\sum_{i=1}^{n} \frac{\left| y_i^P - y_i \right|}{y_i} \right) / n \quad (8)$$

$$\mathrm{RMSE} = \sqrt{\left(\sum_{i=1}^{n}\left(y_i^p - y_i\right)^2\right)/n} \tag{9}$$

$$R^2 = 1 - \frac{\sum_{i=1}^{n}\left(y_i - y_i^p\right)^2}{\sum_{i=1}^{n}(y_i - \bar{y})^2} \tag{10}$$

where y_i^p is the predicted AGB of the ith plot, y_i is the reference AGB of the ith plot, $\bar{y}$ is the mean of the true values, and n is the number of samples in the test set.

Based on the full factorial experimental results (4 data types × 4 sampling methods × 4 statistical models = 64 combinations), the optimal combination was identified using R^2 maximization as the primary criterion and RMSE minimization as the secondary criterion. MAE and MRE were also reported as supplementary metrics to provide a more comprehensive evaluation of model errors. The best-performing combination of inventory data alone—rather than a fixed model or CV method—was used as the baseline. This baseline represents the best possible accuracy achievable using only ground-based inventory information (stand age and canopy cover), without relying on any remote sensing or meteorological data. The performance of all other combinations was then compared against this baseline to quantify the marginal improvements brought by incorporating additional data sources.

All experiments were conducted in a Python 3.9 environment, with modeling and evaluation implemented using the Scikit-learn library [31].

2.4. Uncertainty Analysis

To gain deeper insights into the contributions of different factors to estimation errors and the distribution patterns of prediction reliability, this study conducted uncertainty analysis at two levels.

2.4.1. Variance Decomposition Assessment

To quantitatively evaluate the contribution of each factor to estimation errors at the experimental design level, a three-way Analysis of Variance (ANOVA) was performed on RMSE. Using data type, statistical model, cross-validation method, and their interaction effects as independent variables, and the mean RMSE as the dependent variable, an ordinary least squares (OLS) linear model was constructed as follows:

RMSE_mean C(DataType) + C(Model) + C(CV_Method) + C(DataType):C(Model) + C(DataType):C(CV_Method) + C(Model):C(CV_Method)

The contribution rate of each factor to the total variation in RMSE across the experimental combinations was quantified by calculating the percentage of each factor's sum of squares relative to the total sum of squares. The same variance decomposition analysis was also applied to MAE, MRE, and R^2.

2.4.2. Residual Distribution Analysis

To further investigate the distributional characteristics of prediction errors across different data combinations, we collected prediction residuals for each data type. Based on the full factorial experimental results, we adopted Random Forest (RF) as the unified model, combined with 10-repetition ShuffleSplit validation, and applied it separately to the four data types (Inventory, Landsat, Inv_Landsat, and Inv_Landsat_Climate), recording the residuals for each test sample. To examine the distribution of errors across different biomass levels, the plots were classified into three classes based on true AGB: low (<50 t/ha), medium (50–150 t/ha), and high (>150 t/ha) [32,33]. Two types of boxplots were then generated: (1) residuals grouped by data type, to compare the central tendency and dispersion of errors across different data combinations; and (2) residuals grouped by both biomass class and data type, to identify error patterns in high-biomass regions. By analyzing the direction of residual skewness (positive skew indicating underestimation, negative skew indicating overestimation) and its variation across biomass levels, we assessed the ability of different data combinations to correct prediction bias.

3. Results

3.1. Variable Selection and Correlation Analysis

In order to screen the candidate predictive variables for AGB estimation and avoid circular argument, the variables used to construct the reference AGB (i.e., tree height *H* and *DBH*) were excluded from the correlation analysis. Figure 4 shows the correlation coefficients between the remaining candidate variables and the reference AGB. The direct correlations between meteorological variables and the reference AGB were relatively low, with all correlation values below 0.3 (Figure 4A).

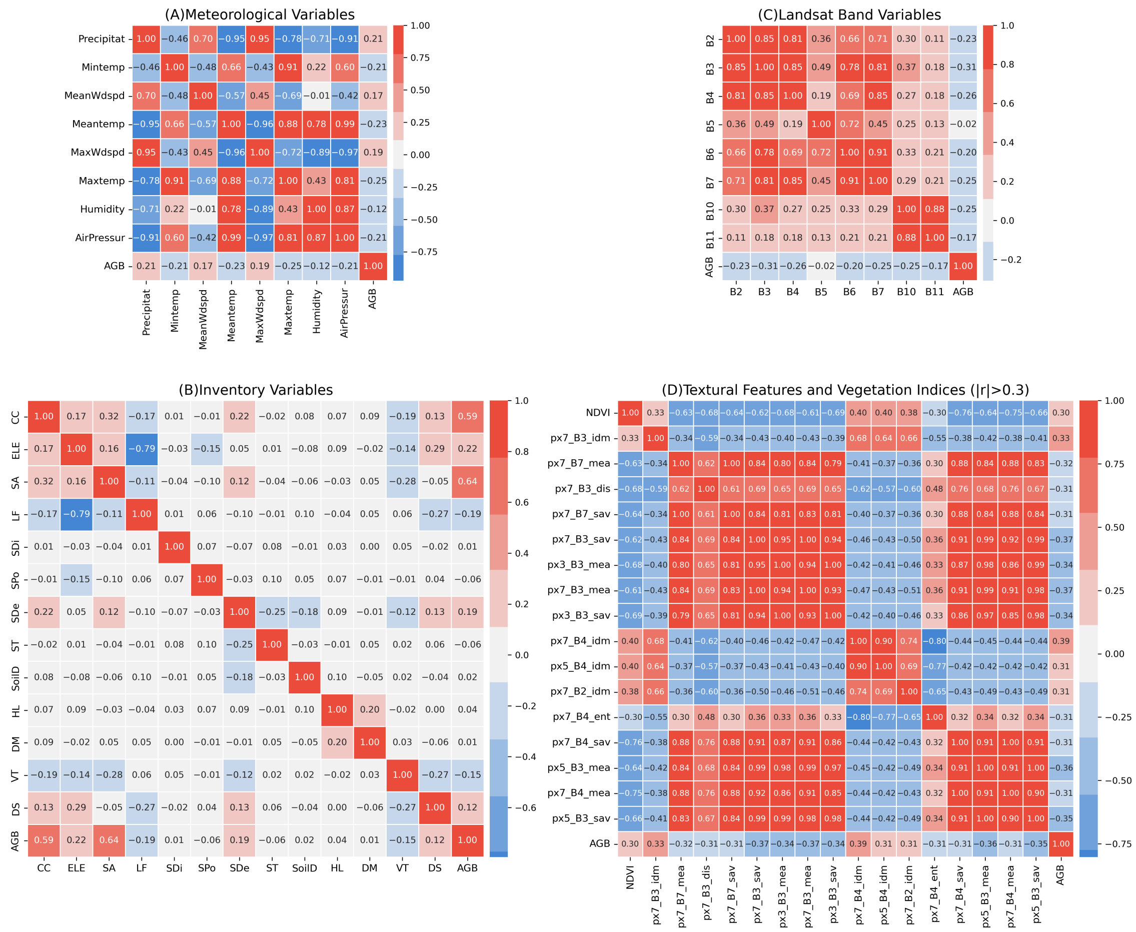

Figure 4. Correlation of candidate variables with forest reference AGB. (**A**) Meteorological variables; (**B**) forest inventory variables; (**C**) Landsat band variables; (**D**) textural features and vegetation indices. Red indicates positive correlation; blue indicates negative correlation. Precipitat = precipitation, Mintemp = minimum temperature, MeanWdspd = mean 2 min wind speed, Meantemp = mean temperature, MaxWdspd = maximum wind speed, Maxtemp = maximum temperature, Humidity = Mean relative humidity, AirPressur = air pressure. CC = canopy cover, ELE = elevation, SA = stand age, LF = landform, SDi = slope direction, SPo = slope position, SDe = degree of slope, ST = soil type, SoilD = soil depth, HL = humus layer thickness, DM = forest litter depth, VT = vegetation type, DS = dominant species.

Among the forest inventory variables (Figure 4B), forest age (SA) and canopy cover (CC) showed the strongest positive correlation with AGB (0.59–0.64). In contrast, other candidate variables exhibited generally low correlations with AGB. The degree of slope (SDe) had a relatively higher positive correlation (0.19), while landform (LF) showed a weak negative correlation (−0.19), and vegetation type (VT) exhibited a weak negative correlation (−0.15), which reflects the categorical nature of this variable (see the note in Table 2). The correlation between all soil property variables and the reference AGB was very low ($|r| < 0.1$), indicating their limited predictive potential in this study system. The correlation results between the variables of Landsat 8 band data and the reference AGB are depicted in Figure 4C. Among the bands, B3 exhibited the strongest negative correlation with the reference AGB (−0.31), followed by B4 (−0.26) and B7 and B10 (both −0.25), while the absolute correlation values of the remaining bands were all below 0.25. Due to the numerous texture feature variables, ALOS variables and vegetation indices variables, only variables with correlations exceeding 0.3 are presented in Figure 4D.

Finally, variables with absolute Pearson correlation coefficients ($|r|$) ≥ 0.30 were retained for subsequent modeling. The Pearson correlation coefficients and significance levels of the retained variables are summarized in Table 7. All retained variables showed statistically significant correlations with reference AGB ($p < 0.05$). Additionally, all meteorological variables were included as independent variables in constructing the model for the fourth data type (Forest inventory data + Remote sensing data + Meteorological data). In addition, Supplementary Material S1 provides the correlation analysis results between all candidate variables and AGB.

Table 7. Selected independent variables with $|r| \geq 0.30$ and their Pearson correlation coefficients with reference AGB.

Variable	Correlation	Variable	Correlation
	Inventory variables		
Stand age (SA)	0.64 ***	Canopy cover (CC)	0.59 ***
	Landsat band and vegetation index		
B3	−0.31 ***	NDVI	0.30 ***
	Textural features		
px7_B4_idm	0.39 ***	px7_B3_mea	−0.37 ***
px7_B3_sav	−0.37 ***	px5_B3_mea	−0.36 ***
px5_B3_sav	−0.35 ***	px3_B3_sav	−0.34 ***
px3_B3_mea	−0.34 ***	px7_B3_idm	0.33 ***
px7_B7_mea	−0.32 ***	px7_B2_idm	0.31 ***
px5_B4_idm	0.31 ***	px7_B4_mea	−0.31 ***
px7_B7_sav	−0.31 ***	px7_B3_dis	−0.31 ***
px7_B4_ent	−0.31 ***	px7_B4_sav	−0.31 ***

*** $p < 0.001$; NDVI = normalized difference vegetation index. Meteorological and topographic variables did not meet the $|r| \geq 0.30$ threshold but were still included in the Inv_Landsat_Climate data combination (see Section 2.2.5).

3.2. Accuracy Comparison Based on Cross-Validation

Figure 5 shows the R^2 results of forest biomass estimation under all combinations (data type × model × CV method). Under the four CV modes, linear regression, MLP and random forest (RF) consistently outperformed SVR in terms of R^2. By comparing the four data types, the R^2 accuracy of the single-Landsat mode was poor (generally lower than 0.20), while the other three modes containing inventory data differed little.

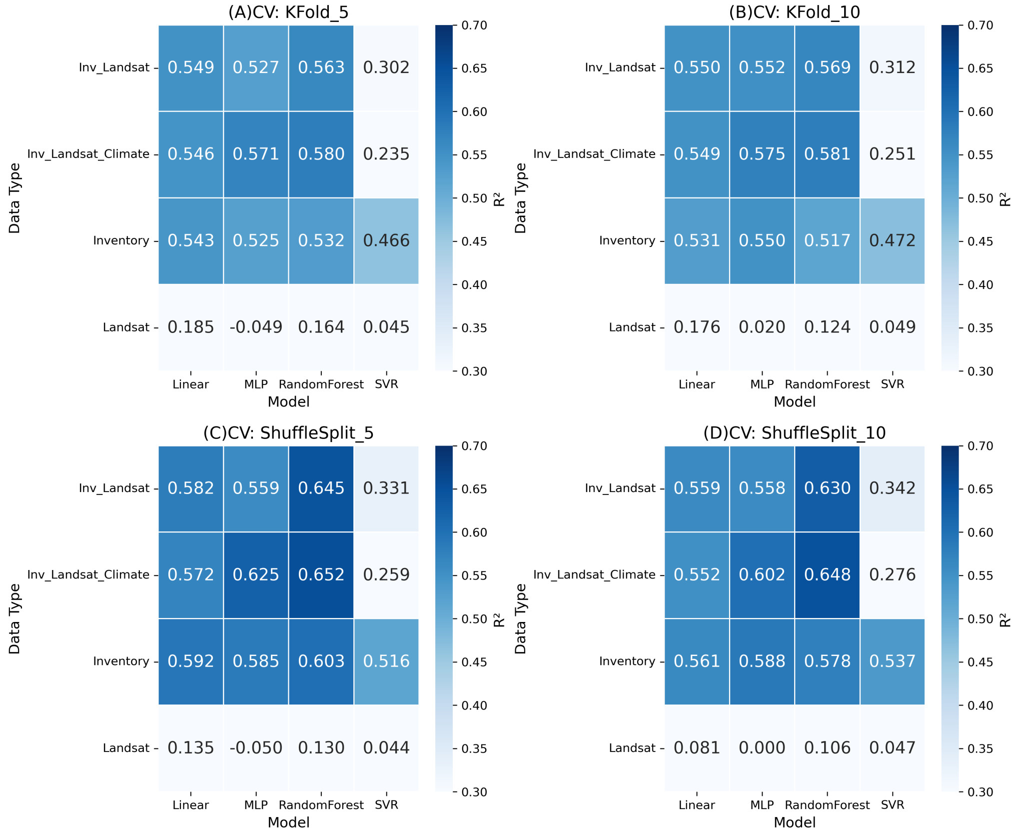

Figure 5. R^2 Comparison: data type × model × CV method.

Figure 6 shows the RMSE distribution under all combinations; Figure 7 shows the overall distribution of MAE and MRE under different data × models as box plots. The trends of RMSE, MAE and MRE were broadly consistent: the error under Landsat-only data was higher than the other three groups, and the error range (MRE dispersion) was larger; the error distribution of MLP was the most unstable in Landsat-only mode.

From the comprehensive view of the four evaluation indicators, the following results can be obtained: (1) The model using only inventory data already achieved satisfactory accuracy. For example, the best inventory-based configuration (Inventory + RandomForest + ShuffleSplit_5) achieved R^2 = 0.60 and RMSE = 35.78 t/ha. (2) Adding Landsat 8 data to inventory data generally improved accuracy, but the magnitude of improvement was modest. In the best-performing combination (Inv_Landsat + RandomForest + ShuffleSplit_5), RMSE decreased from 35.78 t/ha (Inventory + RF + ShuffleSplit_5) to 33.90 t/ha (a reduction of 5.3%), and R^2 increased from 0.60 to 0.64 (an improvement of 6.7%). In some model–CV configurations (e.g., RandomForest + KFold_10), this improvement was statistically significant (Figure 6), but the absolute gain remained limited (approximately 2 to 3 t/ha in RMSE). (3) Further overlay of meteorological data (inv_landsat_climate) produced inconsistent effects across different models. For linear regression and random forest, the changes in accuracy were negligible; for SVR, a slight decline in performance was observed, while for MLP, a modest improvement was obtained. (4) Models that rely solely on optical remote sensing (Landsat 8) had the lowest accuracy and the least stable performance: R^2 was mostly less than 0.20, and the distribution range of MRE was the widest. The goodness-of-fit statistics (R^2, RMSE, MAE, and MRE, with standard deviations across folds) of all 64 combinations are provided in Supplementary Material S2.

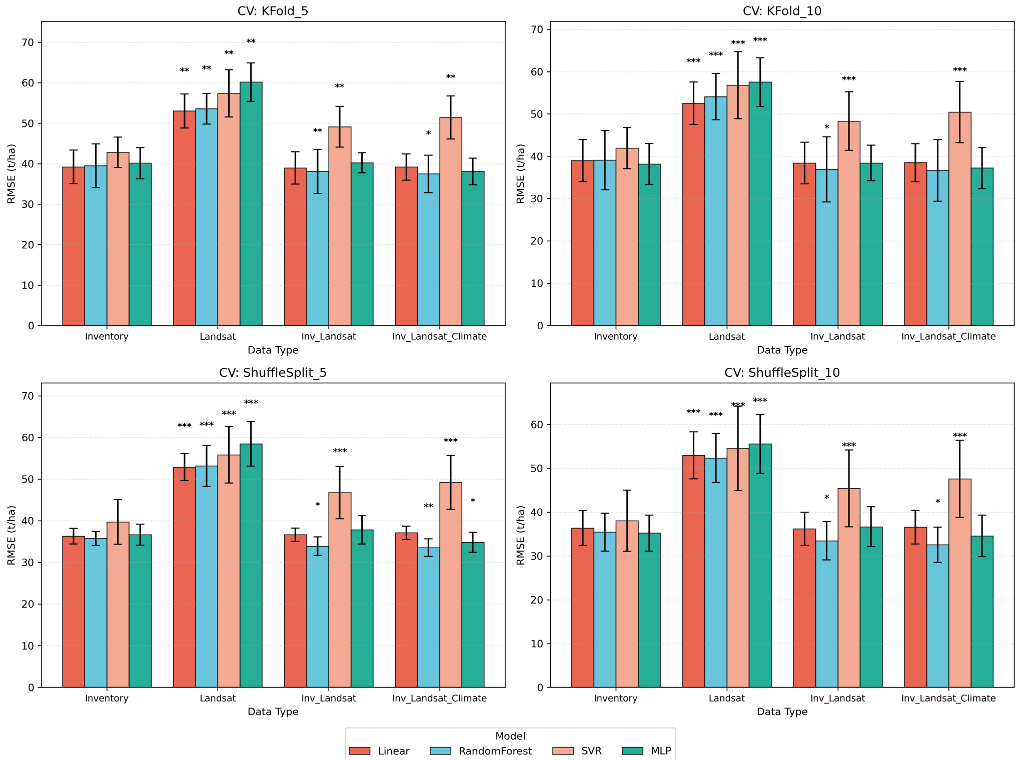

Figure 6. RMSE comparison across data types, models, and CV methods based on 80% training data. Error bars represent ±1 standard deviation across cross-validation folds. Asterisks (*, **, ***) indicate that the corresponding model is significantly different from the inventory-only baseline within the same data type and CV method, based on paired *t*-tests across folds (* $p < 0.05$, ** $p < 0.01$, *** $p < 0.001$).

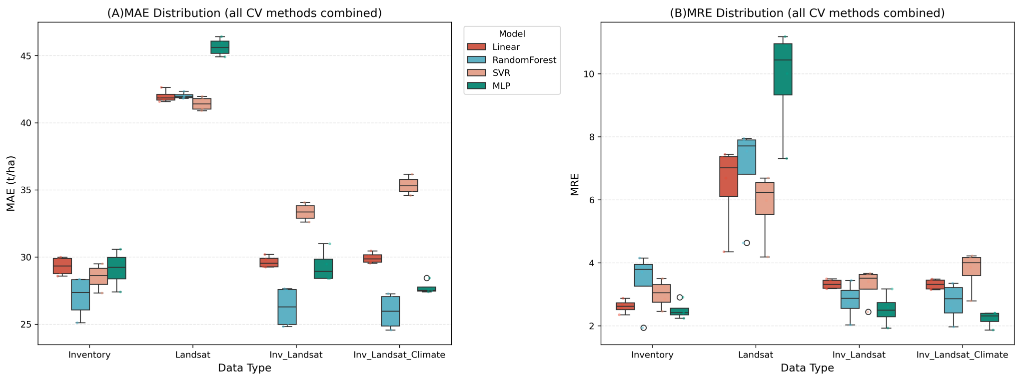

Figure 7. Comparison of forest AGB estimation accuracy between 5-fold and 10-fold.

3.3. External Validation of the Best Model Combination

Based on the cross-validation results, the best-performing model configuration for each data type was identified as follows: Inventory → RandomForest + ShuffleSplit_5; Landsat → Linear + KFold_5; Inv_Landsat → RandomForest + ShuffleSplit_5; and Inv_Landsat_Climate → RandomForest + ShuffleSplit_10. Among these four optima, Inv_Landsat_Climate + Random Forest + ShuffleSplit_10 achieved the best overall cross-validation performance (R^2 = 0.65, RMSE = 32.53 t/ha), followed by Inv_Landsat + Random Forest + ShuffleSplit_5 (R^2 = 0.64, RMSE = 33.90 t/ha) and Inventory + Random Forest + ShuffleSplit_5 (R^2 = 0.60, RMSE = 35.78 t/ha), while the Landsat-only optimum (Linear + KFold_5) performed worst (R^2 = 0.18, RMSE = 53.02 t/ha). Notably, this overall best configuration did not maintain its advantage on the independent test set (R^2 = 0.54), where Inv_Landsat + Random Forest achieved the highest R^2 (0.56).

On the external test set, the optimal combination (Inv_Landsat + RandomForest, Figure 8C) achieved R^2 = 0.56 and RMSE = 40.09 t/ha, corresponding to a 3.7% improvement in R^2 and a 1.8% reduction in RMSE compared to the best Inventory-only configuration (R^2 = 0.54, RMSE = 40.81 t/ha; Figure 8A). However, further incorporating climate data resulted in little additional gain (R^2 = 0.54, RMSE = 41.14 t/ha).

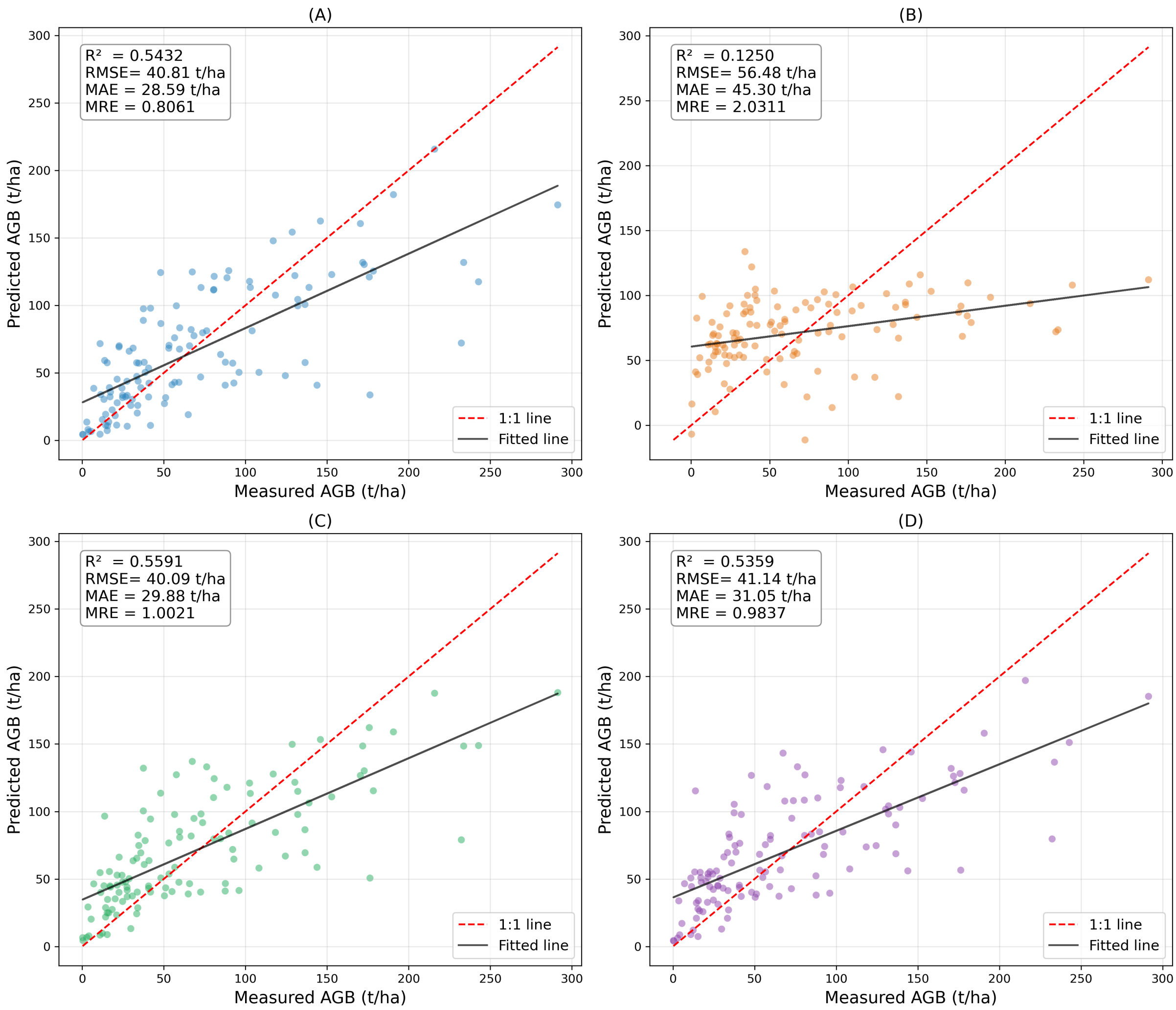

Figure 8. Scatter plots of predicted versus measured AGB on the independent test set for the optimal model under each data type. (**A**) Inventory + RF + ShuffleSplit_5, (**B**) Landsat + Linear + KFold_5, (**C**) Inv_Landsat + RF + ShuffleSplit_5, (**D**) Inv_Landsat_Climate + RF + ShuffleSplit_10. The red dashed line indicates the 1:1 reference line, and the solid black line is the linear fit. Performance metrics (R^2, RMSE, MAE, MRE) are shown in the upper-left corner of each panel.

3.4. Key Factors Influencing Accuracy

The results of the three-way ANOVA are shown in Figure 9; in the factor labels, C() denotes a categorical factor in the ANOVA model. Data type (C(Datatype)) was the most critical influencing factor, contributing 73.0% of the variation in RMSE across the 64 experimental combinations and accounting for more than half of the total variation. Model selection (C(Model)) was a secondary but still important factor, contributing 15.1% of the variation in RMSE. The interaction between data type and model (C(Datatype):C(Model)) contributed 8.5% of the variation in RMSE. The cross-validation method (C(CV_Method)) and its interactions with the other factors contributed very little (each $<$ 3.0%).

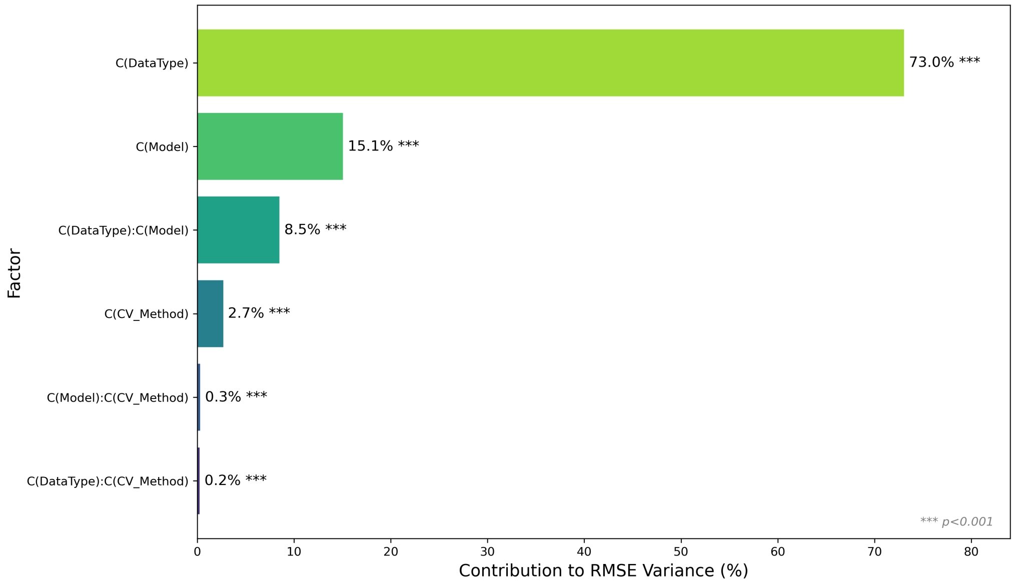

Figure 9. ANOVA decomposition of variation in RMSE across the experimental combinations.

3.5. Residual Distribution

Figure 10 shows the residual distributions of the four data types under the optimal combination (RF + ShuffleSplit_10). The following patterns emerged: Inventory, Inv_Landsat, and Inv_Landsat_Climate all had residuals centered near zero, with broadly symmetric boxes and IQRs approximately spanning -22∼+15 t/ha. The three groups exhibited similar overall bias, indicating that data combinations containing inventory data showed no substantial systematic bias at the aggregate level. The Landsat-only group shifted markedly, with a median of approximately -15 t/ha—the largest deviation from zero among the four groups. This indicated that Landsat alone produced a mild but systematic overestimation (negative residuals, i.e., predicted values exceed observed values).

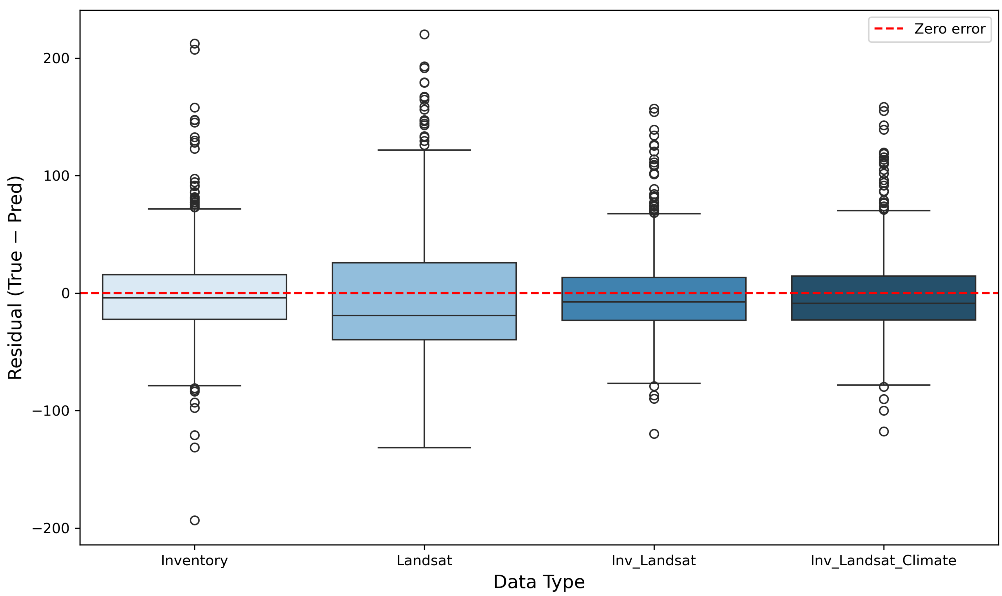

Figure 10. Residual distribution by data type.

Figure 11 displays the residuals stratified by biomass level (Low < 50, Medium 50–150, High > 150 t/ha) and data type (4 groups) under the optimal combination, revealing systematic structural differences in residuals across biomass strata. In the low-biomass stratum (<50 t/ha), the median residuals of all four data types lay below the zero line, indicating a mild systematic overestimation (residual < 0) of low-biomass plots. The Landsat group had the lowest median, exhibiting the most pronounced overestimation. Inventory, Inv_Landsat, and Inv_Landsat_Climate displayed similar medians and IQRs. Several downward outliers reached −100∼−200 t/ha, corresponding to a small number of severely overestimated low-biomass plots. In the medium-biomass stratum (50∼150 t/ha), the boxes of all four data types were nearly perfectly symmetric, with medians close to zero. IQRs generally spanned −25∼+25 t/ha, and whiskers roughly −80∼+110 t/ha, with very few outliers. This stratum was the most stable and least biased part of the prediction space, indicating that the model provided near-unbiased estimates for medium-biomass plots. In the high-biomass stratum (>150 t/ha), the median residuals of all four data types lay substantially above the zero line, indicating a widespread systematic underestimation (residual > 0) of high-biomass plots. The Landsat group showed the most extreme behavior: the highest median together with a narrow IQR. This indicates that, in the high-biomass stratum, Landsat produced a more severe systematic underestimation. Inventory, Inv_Landsat, and Inv_Landsat_Climate exhibited similar medians and IQRs, all smaller than those of Landsat.

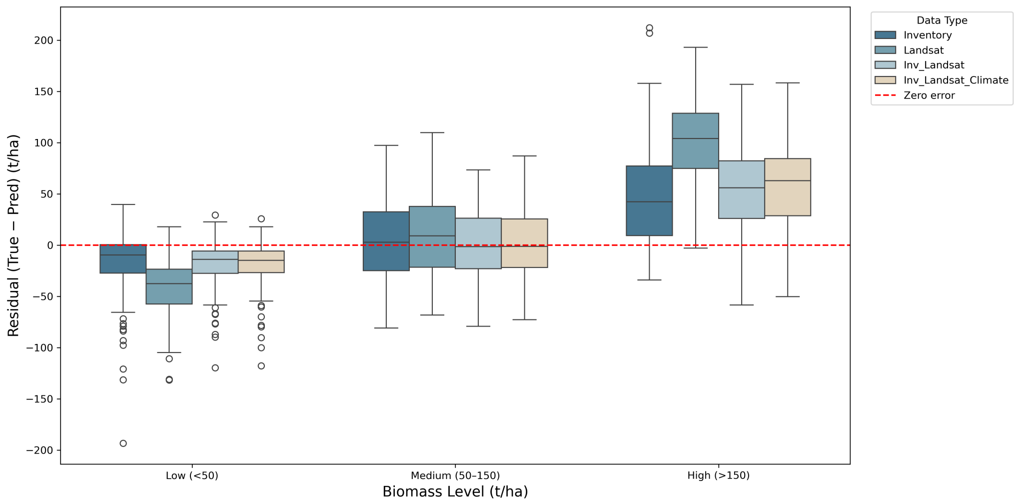

Figure 11. Residual distribution by data type and biomass level.

4. Discussion

4.1. Data Type as the Primary Determinant of Estimation Accuracy

The variance decomposition (Section 3.4) showed that data type alone contributed 73.0% of the variation in RMSE across the 64 experimental combinations, whereas model selection contributed 15.1% and the data type × model interaction 8.5%; the data-partitioning scheme and its interactions each contributed less than 3.0%. This hierarchy is internally consistent with the variable correlation analysis (Section 3.1): stand age and canopy cover were correlated with the reference AGB at 0.64 and 0.59, respectively, whereas no Landsat band exceeded $|r| = 0.31$ and the strongest textural feature reached only 0.39. These two lines of evidence jointly indicate that, at the plot scale, the composition of the input features sets the ceiling of AGB estimation accuracy, while models and sampling strategies can only be optimized within this data-given boundary. A comparable hierarchy was reported by Fassnacht et al. [7], who found that data type and sample size were more decisive for estimation accuracy than the choice of prediction method.

The dominance of inventory data can be explained by the different causal chains linking the two data sources to AGB. Stand age and canopy cover are direct outcomes of forest growth and carbon accumulation processes and therefore encode structural information that is intrinsically coupled with biomass [19]; in addition, canopy cover is strongly shaped by forest management practices such as planting density, thinning, and tending, so that these inventory attributes also implicitly capture management effects that optical reflectance cannot directly observe. In contrast, Landsat reflectance is only indirectly related to AGB: the spectral signal is jointly modulated by canopy structure, understorey background, topography, and phenological stage, and it loses sensitivity in medium- to high-biomass forests owing to signal saturation [15,34,35]. Consistent with this interpretation, Li et al. [8] showed for subtropical forests in central China that incorporating canopy cover substantially improved Landsat 8-based AGB estimation; in other words, optical data become markedly more informative when structural attributes are available alongside them. Our results complement this finding from the opposite direction: when accurate structural attributes from the ground inventory are already available, the additional information provided by optical data is correspondingly small.

The limited and model-dependent effect of the meteorological variables may be attributed to two factors. First, the meteorological variables exhibited low spatial heterogeneity across the study area, which restricted their additional explanatory power at the plot scale. Second, previous studies have shown that stand age and canopy cover are major determinants of vegetation carbon stocks, while climatic conditions and stand structural attributes jointly regulate forest AGB [36,37]. Therefore, after stand age and canopy cover had been included in the models, some of the explanatory information provided by the meteorological variables may have overlapped with that represented by these inventory variables, thereby providing little additional predictive information.

These mechanisms explain the core quantitative results of this study. Using stand age and canopy cover alone, the best configuration reached $R^2 = 0.60$ and RMSE = 35.78 t/ha in cross-validation and $R^2 = 0.54$ on the independent external test set. Adding Landsat 8 increased the external R^2 only to 0.56 (an improvement of 3.7%, with an RMSE reduction of 1.8%), and the further addition of meteorological data provided no gain ($R^2 = 0.54$). Under identical model and cross-validation settings, the RMSE reduction achieved by adding Landsat 8 was about 5.3% at best; although this improvement reached statistical significance in some configurations (e.g., RF + KFold_10), the absolute gain remained within 2–3 t/ha. This pattern reflects a clear state of diminishing returns: the information content of the inventory data is already close to the saturation point of plot-scale AGB estimation under the conditions examined here. This finding does not negate the value of data fusion; rather, it identifies a boundary condition for its utility, echoing the concerns raised regarding large-scale optical-based biomass estimates [17,18]. Under the conditions examined in this study, where a systematic and high-quality ground monitoring system was already available, incorporating additional data sources and increasing modeling complexity yielded only limited improvements in plot-scale AGB estimation accuracy. The marginal contribution of optical remote sensing evidently depends on the availability and quality of the existing ground information, as also suggested by Fassnacht et al. [7]. Nevertheless, the present findings are specific to the forest conditions, plot scale, temporal setting, inventory predictors, and modeling approaches examined in Longyan and should not be generalized to other applications of optical remote sensing.

4.2. The Relative Roles of Model Choice and Sampling Strategy

Model selection was the second most important factor, contributing 15.1% of the variation in RMSE. Across all data combinations, linear regression, random forest (RF), and multi-layer perceptron (MLP) consistently outperformed support vector regression (SVR), while the gap between the linear model and RF remained small. This pattern is consistent with the characteristics of the present dataset (590 plots and weakly nonlinear feature–AGB relationships): linear and tree-based models are comparatively robust under moderate sample sizes, whereas SVR is sensitive to kernel and regularization settings, and single-hidden-layer neural networks generally require larger samples to converge stably [38,39]. Similar observations were reported by Were et al. [38], who found RF to outperform both SVR and artificial neural networks for the spatial prediction of soil organic carbon, and RF is known to be relatively insensitive to its default hyperparameters [40,41]. The pronounced instability of MLP in the Landsat-only mode further suggests that the limiting factor was the weak and noisy spectral–AGB relationship rather than the model class itself. It should nevertheless be acknowledged that the hyperparameter search conducted here, while systematic, was restricted to a single predefined grid per algorithm. More extensive strategies, e.g., randomized search over broader ranges, Bayesian optimization, or nested cross-validation, could in principle identify different optimal settings and thereby alter the relative ranking among models. Two observations, however, support the robustness of our main conclusion: first, the linear regression model, whose results are independent of hyperparameter choice, performed comparably to RF and MLP, and second, the model ranking remained stable across all four data types and across both cross-validation schemes.

Our results both echo and differ from Fassnacht et al. [7]. They likewise reported the prediction method as the second most important factor and found a marked advantage of RF over stepwise linear regression, which agrees with the overall ranking observed here. The smaller linear–RF gap in our study can be attributed to the nature of the predictors: their study relied on LiDAR and hyperspectral data, whose relationships with biomass are strongly nonlinear, whereas the relationships between our input variables (stand age, canopy cover, spectral and textural features) and AGB are close to linear or only weakly nonlinear, a situation in which differences between model classes naturally narrow. In addition, our sample size (590 plots) is larger than the effective sample sizes of their German (297) and Chilean (150) sites; larger samples help narrow the performance gap between models by alleviating the overfitting of more complex algorithms [7,42]. Moreover, the significant data type $\times$ model interaction (8.5%) indicates that the optimal model may differ among data types, suggesting that model comparison remains necessary for each data combination in practice, rather than applying a single model universally.

The data-partitioning scheme contributed less than 3.0% of the variation, indicating that, given the sample size and plot distribution of this study, the difference between KFold and ShuffleSplit imposes little constraint on accuracy. In practical terms, the validation scheme can therefore be selected according to computational cost and replication requirements without materially affecting the results. One caveat deserves mention, however: both schemes are random resampling procedures. For spatially distributed inventory plots, random splits tend to yield optimistic accuracy estimates, because nearby plots share forest conditions, management history, and terrain, so that validation plots remain similar to training plots [43,44]. The systematic 4 km $\times$ 6 km grid on which the FRIC plots are arranged reduces, but does not eliminate, such spatial dependence. The negligible contribution of the partitioning factor should therefore be interpreted as a comparison between two random resampling schemes, rather than as evidence that spatially blocked validation would yield equivalent accuracy.

4.3. Residual Patterns Across Biomass Strata: Saturation and Regression to the Mean

The residual analysis (Section 3.5) provides a stratum-level perspective that aggregate accuracy metrics cannot offer. At the aggregate level, the three inventory-containing combinations produced residuals centered near zero with broadly symmetric boxes (IQRs of approximately -22 to $+15$ t/ha), indicating no substantial systematic bias, whereas the

Landsat-only model exhibited a median of approximately −15 t/ha—the largest deviation from zero among the four configurations, i.e., a mild but systematic overestimation. More importantly, the stratified residuals displayed a coherent two-tail-biased structure: low-biomass plots were systematically overestimated, medium-biomass plots were nearly unbiased, and high-biomass plots were systematically underestimated for all four data types.

This structure is a typical signature of regression to the mean (shrinkage): models anchor their predictions near the center of the training distribution, producing near-unbiased estimates where samples are dense (the medium stratum, which contains most plots) and pulling predictions toward the mean at both tails. Analogous patterns have been documented repeatedly in AGB mapping. Ploton et al. [45] showed that the predictive performance of large-scale biomass maps deteriorates precisely in the high-biomass range, where the largest stocks are underestimated, and Mitchard et al. [46] reported markedly lower carbon density estimates from satellites than from ground plots in high-biomass Amazonian forests. Our results demonstrate that the same failure mode operates even at the plot scale and even when inventory predictors are used, and that it is amplified when only optical data are available.

The Landsat-only model displayed the most extreme behavior in the high-biomass stratum: the largest median underestimation, extreme outliers exceeding +200 t/ha, but simultaneously a narrow IQR. In other words, this model was not merely inaccurate but systematically and consistently biased at high biomass—a failure mode that aggregate RMSE or R^2 values would largely conceal. This behavior is consistent with the well-documented saturation of optical signals in medium- and high-biomass forests: above saturation levels of roughly 100–150 t/ha in dense subtropical forests, spectral reflectance and vegetation indices lose sensitivity to further biomass increases [16,34,35], precisely where accurate estimates matter most for carbon accounting.

These observations carry two practical implications. First, residual diagnostics stratified by biomass level should accompany aggregate accuracy metrics in AGB studies, because models with similar RMSE values can hide opposite bias structures across strata; stratified error reporting has likewise been advocated in uncertainty propagation studies [47,48]. Second, it should be noted that even the best configuration left approximately 44% of the plot-level variation unexplained on the external test set ($R^2 = 0.56$); this model-related unexplained variance is conceptually distinct from the ANOVA decomposition of the variation in RMSE across experimental combinations presented in Section 3.4. Moreover, prediction uncertainty encompasses several distinct components—including reference-data error, model bias, and residual dispersion—that cannot be captured by any single metric. The residual-based diagnostics used here quantify bias and error dispersion and should therefore be reported alongside, rather than instead of, aggregate accuracy metrics.

4.4. Limitations and Future Perspectives

Based on the comparison of the 64 modeling combinations, the combination of forest inventory data, Landsat 8 data, and meteorological data with the Random Forest model and 10-repeat ShuffleSplit validation achieved the best overall performance under the conditions examined in this study. This result provides a specific modeling strategy for improving plot-scale AGB estimation in Longyan. For other subtropical forest regions with similar forest types, stand structures, topographic and climatic conditions, and comparable data availability, this configuration may serve as an initial reference for model development and strategy selection. However, both the identified optimal configuration and the limited marginal gain from Landsat 8 should be regarded as context-specific results determined by the sample characteristics, environmental conditions, data sources, spatial scale, temporal setting, and candidate methods examined here, rather than as universally applicable conclusions. Direct application to regions with substantially different ecological conditions, inventory systems, remote sensing data, or spatial scales may therefore introduce bias, and local recalibration and independent validation remain necessary. In addition, the limited representation of high-biomass plots and the restricted range of remote sensing data and models are important limitations of this study. Future research should increase the representation of high-biomass forests, incorporate multi-temporal and structure-sensitive remote sensing data such as LiDAR or radar, whose synergy with optical data has been demonstrated in previous studies [4,49,50], explore alternative modeling strategies, and further improve the assessment of prediction uncertainty and model transferability.

Furthermore, all validation schemes adopted in this study are based on random resampling. Spatially or environmentally blocked validation designs [43,44,51] would provide a stricter test of spatial transferability and should be considered in future work, particularly when models are extrapolated beyond the sampled inventory plots.

5. Conclusions

This study evaluated the marginal contribution of optical remote sensing data to plot-scale AGB estimation when high-quality forest inventory data (stand age and canopy cover) were already available, using a full factorial design of 4 data types × 4 cross-validation methods × 4 statistical models (64 combinations) in Longyan, Fujian Province. Three research questions and their corresponding hypotheses were posed at the end of the Introduction; the answers based on the cross-validation and external test results are summarized below.

(RQ1, H1) When high-quality inventory predictors were already available at the plot scale, the marginal effect of adding Landsat 8 optical data (and subsequently meteorological data) on AGB estimation accuracy was limited, model-dependent, and not statistically significant in the majority of model configurations (paired *t*-tests, Figure 6): linear regression showed no significant change; Random Forest exhibited a statistically significant but quantitatively small RMSE reduction; SVR was actually degraded by the addition of remote sensing data; and MLP remained unchanged in most configurations, with a significant improvement only in the single case where meteorological data were added. Under identical model and validation settings, the best inventory-only configuration achieved $R^2 = 0.60$ and RMSE = 35.78 t/ha, and the corresponding Inv_Landsat configuration $R^2 = 0.64$ and RMSE = 33.90 t/ha (RMSE −5.3%, R^2 + 6.7%); the further addition of meteorological data provided no consistent gain. H1 is therefore supported: the improvement was limited in magnitude and statistically insignificant in most configurations, while the direction of the marginal effect varied with the model.

(RQ2, H2) Three-way ANOVA (Figure 9) showed that data type dominated the variation in RMSE across the 64 combinations (73.0%), far exceeding the contributions of model choice (15.1%) and the data type × model interaction (8.5%), whereas the cross-validation design contributed negligibly (<3.0%). H2 is therefore supported.

(RQ3, H3) Residual analysis (Figures 10 and 11) revealed a systematic two-tailed bias—overestimation of low-biomass plots and underestimation of high-biomass plots—with the most severe bias occurring in the high-biomass stratum, and the Landsat-only configuration exhibiting the most pronounced deviation of the median residual from zero at both biomass extremes and at the aggregate level. H3 is therefore supported.

Across the four data-type optima, Inv_Landsat_Climate + Random Forest + ShuffleSplit_10 achieved the best overall cross-validation performance ($R^2 = 0.65$, RMSE = 32.53 t/ha); on the independent external test set (Figure 8), however, the best-performing combination was Inv_Landsat + Random Forest ($R^2 = 0.56$, RMSE = 40.09 t/ha), leaving approximately 44% of the plot-level variation unexplained, and the cross-validation optimum did not retain its advantage on the external set. Overall, these findings suggest that, under the specific forest conditions, data configuration, and spatial scale examined in this study, optical remote sensing provided only modest additional predictive information beyond the available inventory data. In regions with well-established ground inventory systems, the marginal accuracy gains from integrating additional optical and meteorological data should therefore be weighed explicitly against the added complexity, and improving the representation of under-sampled high-biomass stands may be a more effective path toward reducing estimation uncertainty than further data fusion alone.

Supplementary Materials: The following supporting information can be downloaded at: https://www.mdpi.com/article/10.3390/f17091094/s1, Suplementary Material S1: Correlation coefficients of all candidate variables with reference AGB; Suplementary Material S2: Goodness-of-fit statistics of all 64 combinations.

Author Contributions: Conceptualization, X.Z. and Y.S.; methodology—formal analysis and investigation, X.Z., Y.S. and Y.W.; resources, Y.R.; writing—original draft preparation, X.Z. and Y.S.; writing—review and editing, X.Z., Y.S., Y.C., G.L. and S.D.; visualization, X.Z.; funding acquisition, Y.R. All authors have read and agreed to the published version of the manuscript.

Funding: This research was funded by Fujian Provincial Department of Science and Technology (2024I0029, 2026J002049), National Key Research Program of China (2022YFF1303001), Fujian Provincial Department of Education (JAT220354), Sanming University (22YG15, PYT2307), National Natural Science Foundation of China (42001210, 31972951, 31670645, 42171100, 41801182, and 41807502), National Social Science Fund (17ZDA058), Fujian Provincial Department of S&T Project (2022T3047, 2021I0041, 2021T3058, 2019J01136), the Strategic Priority Research Program of the Chinese Academy of Sciences (XDA23020502), Xiamen S&T Project (3502Z20226016). We would like to express our sincere gratitude to the anonymous reviewers for their constructive feedback and valuable suggestions.

Data Availability Statement: This study's datasets are available upon request from the corresponding author.

Acknowledgments: We thank the anonymous reviewers for their constructive comments and recommendations.

Conflicts of Interest: The authors declare no conflict of interest. The funders had no role in the design of the study; in the collection, analyses, or interpretation of data; in the writing of the manuscript; or in the decision to publish the results.

Abbreviations

The following abbreviations are used in this manuscript:

AGB	Aboveground Biomass
NDVI	Normalized Difference Vegetation Index
RF	Random Forest
SVR	Support Vector Regression
MLP	Multi-Layer Perceptron
FRIC	Forest Resource Inventory of China
GEE	Google Earth Engine
H	Tree Height
DBH	Diameter at Breast Height
MAE	Mean Absolute Error
MRE	Mean Relative Error
RMSE	Root Mean Square Error

Appendix A

Table A1. Allometric equations for calculating single-tree AGB. All equations were developed in a previous study by the authors [22].

Serial Number	Categories	Allometric Equation	R^2	*p* Value	Bias%	Standard Error	Number of Trees
1	Conifers	AGB = 0.0318 $(DBH^2H)^{0.9487}$	0.987	7.69×10^{-5}	0.65	8.95	19
2	*Fagaceae*	AGB = 0.0592 $(DBH^2H)^{0.9475}$	0.962	6.33×10^{-12}	3.16	42.63	93
3	*Styracaceae*	AGB = 0.0407 $(DBH^2H)^{0.9406}$	0.956	0.0001	2.49	25.03	19
4	*Elaeocarpaceae*	AGB = 0.0684 $(DBH^2H)^{0.8846}$	0.934	2.03×10^{-7}	4.05	19.08	23
5	*Lauraceae*	AGB = 0.1267 $(DBH^2H)^{0.8361}$	0.973	0.0047	1.72	16.58	20
6	*Magnoliaceae*	AGB = 0.0781 $(DBH^2H)^{0.8737}$	0.954	0.0038	4.05	33.41	20
7	*Daphniphyllaceae*	AGB = 0.0725 $(DBH^2H)^{0.9001}$	0.971	0.0016	2.22	32.01	20
8	*Juglandaceae*	AGB = 0.0664 $(DBH^2H)^{0.8895}$	0.854	0.0004	9.26	18.17	19
9	Other broad-leaved species	AGB = 0.0819 $(DBH^2H)^{0.8765}$	0.939	7.45×10^{-10}	4.89	22.2	223

References

1. Houghton, R.; Hall, F.; Goetz, S. Importance of biomass in the global carbon cycle. *J. Geophys. Res. Atmos.* **2009**, *114*, G00E03. [CrossRef]
2. Huang, H.; Liu, C.; Wang, X.; Zhou, X.; Gong, P. Integration of multi-resource remotely sensed data and allometric models for forest aboveground biomass estimation in China. *Remote Sens. Environ.* **2019**, *221*, 225–234. [CrossRef]
3. Fassnacht, F.E.; Latifi, H.; Hartig, F. Using synthetic data to evaluate the benefits of large field plots for forest biomass estimation with LiDAR. *Remote Sens. Environ.* **2018**, *213*, 115–128. [CrossRef]
4. Hu, T.; Su, Y.; Xue, B.; Liu, J.; Zhao, X.; Fang, J.; Guo, Q. Mapping global forest aboveground biomass with spaceborne LiDAR, optical imagery, and forest inventory data. *Remote Sens.* **2016**, *8*, 565. [CrossRef]
5. Zhang, J.; Huang, S.; Hogg, E.; Lieffers, V.; Qin, Y.; He, F. Estimating spatial variation in Alberta forest biomass from a combination of forest inventory and remote sensing data. *Biogeosciences* **2014**, *11*, 2793–2808. [CrossRef]
6. Hogland, J.; Anderson, N.; Peter, J.S.; Drake, J.; Medley, P. Mapping Forest Characteristics at Fine Resolution across Large Landscapes of the Southeastern United States Using NAIP Imagery and FIA Field Plot Data. *ISPRS Int. J. Geo-Inf.* **2018**, *7*, 140. [CrossRef]
7. Fassnacht, F.; Hartig, F.; Latifi, H.; Berger, C.; Hernández, J.; Corvalán, P.; Koch, B. Importance of sample size, data type and prediction method for remote sensing-based estimations of aboveground forest biomass. *Remote Sens. Environ.* **2014**, *154*, 102–114. [CrossRef]
8. Li, C.; Li, Y.; Li, M. Improving forest aboveground biomass (AGB) estimation by incorporating crown density and using landsat 8 OLI images of a subtropical forest in Western Hunan in Central China. *Forests* **2019**, *10*, 104. [CrossRef]
9. Yan, F.; Wu, B.; Wang, Y. Estimating spatiotemporal patterns of aboveground biomass using Landsat TM and MODIS images in the Mu Us Sandy Land, China. *Agric. For. Meteorol.* **2015**, *200*, 119–128. [CrossRef]
10. Tian, L.; Wu, X.; Tao, Y.; Li, M.; Qian, C.; Liao, L.; Fu, W. Review of remote sensing-based methods for forest aboveground biomass estimation: Progress, challenges, and prospects. *Forests* **2023**, *14*, 1086. [CrossRef]
11. Khan, M.N.; Tan, K.; Gul, A.A.; Abbas, S.; Wang, J. Forest aboveground biomass estimation and inventory: Evaluating remote sensing-based approaches. *Forests* **2024**, *15*, 1055. [CrossRef]
12. Miller, G.J.; Morris, J.T.; Wang, C. Estimating aboveground biomass and its spatial distribution in coastal wetlands utilizing planet multispectral imagery. *Remote Sens.* **2019**, *11*, 2020. [CrossRef]
13. Belloli, T.F.; Guasselli, L.A.; Kuplich, T.M.; Ruiz, L.F.C.; de Arruda, D.C.; Etchelar, C.B.; Simioni, J.D. Estimation of aboveground biomass and carbon in palustrine wetland using bands and multispectral indices derived from optical satellite imageries PlanetScope and Sentinel-2A. *J. Appl. Remote Sens.* **2022**, *16*, 034516. [CrossRef]
14. Hemati, M.; Mahdianpari, M.; Shiri, H.; Mohammadimanesh, F.; Salehi, B.; Wu, J. Advancing wetland aboveground biomass mapping: Insights from high-resolution PlanetScope data in the Mississippi River Delta. *Remote Sens. Appl. Soc. Environ.* **2025**, *38*, 101604. [CrossRef]
15. Wu, Y.; Ou, G.; Huang, T.; Zhang, X.; Liu, C.; Liu, Z.; Yu, Z.; Luo, H.; Lu, C.; Shi, K.; et al. Climate interprets saturation value variations better than soil and topography in estimating oak forest aboveground biomass using Landsat 8 OLI imagery. *Remote Sens.* **2024**, *16*, 1338. [CrossRef]
16. Sa, R.; Nie, Y.; Chumachenko, S.; Fan, W. Biomass estimation and saturation value determination based on multi-source remote sensing data. *Remote Sens.* **2024**, *16*, 2250. [CrossRef]

17. Baccini, A.; Walker, W.; Carvalho, L.; Farina, M.; Sulla-Menashe, D.; Houghton, R. Tropical forests are a net carbon source based on aboveground measurements of gain and loss. *Science* **2017**, *358*, 230–234. [CrossRef] [PubMed]
18. Hansen, M.C.; Potapov, P.; Tyukavina, A. Comment on "Tropical forests are a net carbon source based on aboveground measurements of gain and loss". *Science* **2019**, *363*, eaar3629. [CrossRef] [PubMed]
19. Ma, W.; Domke, G.M.; D'Amato, A.W.; Woodall, C.W.; Walters, B.F.; Deo, R.K. Using matrix models to estimate aboveground forest biomass dynamics in the eastern USA through various combinations of LiDAR, Landsat, and forest inventory data. *Environ. Res. Lett.* **2018**, *13*, 125004. [CrossRef]
20. Fang, J.; Chen, A.; Peng, C.; Zhao, S.; Ci, L. Changes in forest biomass carbon storage in China between 1949 and 1998. *Science* **2001**, *292*, 2320–2322. [CrossRef] [PubMed]
21. Brown, S. Measuring carbon in forests: Current status and future challenges. *Environ. Pollut.* **2002**, *116*, 363–372. [CrossRef] [PubMed]
22. Zheng, X. Research on Improving the Accuracy of Subtropical Forest Biomass Estimation Based on Integration Technology. Ph.D. Dissertation, University of Chinese Academy of Sciences, Beijing, China, 2022.
23. Li, L.; Zhang, Q.; Huang, D. A review of imaging techniques for plant phenotyping. *Sensors* **2014**, *14*, 20078–20111. [CrossRef] [PubMed]
24. Wu, C.; Shen, H.; Wang, K.; Shen, A.; Deng, J.; Gan, M. Landsat imagery-based above ground biomass estimation and change investigation related to human activities. *Sustainability* **2016**, *8*, 159. [CrossRef]
25. Huete, A.R. A soil-adjusted vegetation index (SAVI). *Remote Sens. Environ.* **1988**, *25*, 295–309. [CrossRef]
26. Haralick, R.M.; Shanmugam, K.; Dinstein, I.H. Textural features for image classification. *IEEE Trans. Syst. Man Cybern.* **1973**, *SMC-3*, 610–621. [CrossRef]
27. Kelsey, K.C.; Neff, J.C. Estimates of aboveground biomass from texture analysis of landsat imagery. *Remote Sens.* **2014**, *6*, 6407–6422. [CrossRef]
28. Mauya, E.W.; Hansen, E.H.; Gobakken, T.; Bollandsås, O.M.; Malimbwi, R.E.; Næsset, E. Effects of field plot size on prediction accuracy of aboveground biomass in airborne laser scanning-assisted inventories in tropical rain forests of Tanzania. *Carbon Balance Manag.* **2015**, *10*, 10. [CrossRef] [PubMed]
29. Japan Aerospace Exploration Agency (JAXA). ALOS Global Digital Surface Model ALOS World 3D-30m (AW3D30). 2015. Available online: https://www.eorc.jaxa.jp/ALOS/en/dataset/aw3d30/ (accessed on 8 April 2026).
30. Chen, W.; Sun, L.; Li, Q.; He, L. An interpolation dataset for temperature and precipitation at 1km grid resolution in Chinese mainland for recent 38 years. *Meteorol. Sci. Technol.* **2021**, *49*, 7. (In Chinese)
31. scikit-learn. Cross-Validation: Evaluating Estimator Performance. Available online: https://scikit-learn.org/stable/modules/cross_validation.html (accessed on 2 September 2026).
32. Jiang, X.; Li, G.; Lu, D.; Chen, E.; Wei, X. Stratification-based forest aboveground biomass estimation in a subtropical region using airborne lidar data. *Remote Sens.* **2020**, *12*, 1101. [CrossRef]
33. Su, H.; Shen, W.; Wang, J.; Ali, A.; Li, M. Machine learning and geostatistical approaches for estimating aboveground biomass in Chinese subtropical forests. *For. Ecosyst.* **2020**, *7*, 64. [CrossRef]
34. Asner, G.P. Tropical forest carbon assessment: Integrating satellite and airborne mapping approaches. *Environ. Res. Lett.* **2009**, *4*, 034009. [CrossRef]
35. Lu, D.; Chen, Q.; Wang, G.; Moran, E.; Batistella, M.; Zhang, M.; Vaglio Laurin, G.; Saah, D. Aboveground forest biomass estimation with Landsat and LiDAR data and uncertainty analysis of the estimates. *Int. J. For. Res.* **2012**, *2012*, 436537. [CrossRef]
36. Zhang, T.; Ding, G.; Zhang, J.; Qi, Y. Contributions of biotic and abiotic factors to the spatial heterogeneity of aboveground biomass in subtropical forests: A case study of Guizhou Province. *Sustainability* **2022**, *14*, 10771. [CrossRef]
37. Zeng, W.H.; Zhu, S.D.; Luo, Y.H.; Shi, W.; Wang, Y.Q.; Cao, K.F. Aboveground biomass stocks of species-rich natural forests in southern China are influenced by stand structural attributes, species richness and precipitation. *Plant Divers.* **2024**, *46*, 530–536. [CrossRef] [PubMed]
38. Were, K.; Bui, D.T.; Dick, B.; Singh, B.R. A comparative assessment of support vector regression, artificial neural networks, and random forests for predicting and mapping soil organic carbon stocks across an Afromontane landscape. *Ecol. Indic.* **2015**, *52*, 394–403. [CrossRef]
39. Cracknell, M.J.; Reading, A.M. Geological mapping using remote sensing data: A comparison of five machine learning algorithms, their response to variations in the spatial distribution of training data and the use of explicit spatial information. *Comput. Geosci.* **2014**, *63*, 22–33. [CrossRef]
40. Breiman, L. Random forests. *Mach. Learn.* **2001**, *45*, 5–32. [CrossRef]
41. Probst, P.; Wright, M.N.; Boulesteix, A.L. Hyperparameters and tuning strategies for random forest. *Wiley Interdiscip. Rev. Data Min. Knowl. Discov.* **2019**, *9*, e1301. [CrossRef]
42. Foody, G.M. Sample size determination for image classification accuracy assessment and comparison. *Int. J. Remote Sens.* **2009**, *30*, 5273–5291. [CrossRef]

43. Roberts, D.R.; Bahn, V.; Ciuti, S.; Boyce, M.S.; Elith, J.; Guillera-Arroita, G.; Hauenstein, S.; Lahoz-Monfort, J.J.; Schröder, B.; Thuiller, W.; et al. Cross-validation strategies for data with temporal, spatial, hierarchical, or phylogenetic structure. *Ecography* **2017**, *40*, 913–929. [CrossRef]
44. Valavi, R.; Elith, J.; Lahoz-Monfort, J.J.; Guillera-Arroita, G. BlockCV: An r package for generating spatially or environmentally separated folds for k-fold cross-validation of species distribution models. *Methods Ecol. Evol.* **2018**, *10*, 225–232. [CrossRef]
45. Ploton, P.; Mortier, F.; Réjou-Méchain, M.; Barbier, N.; Picard, N.; Rossi, V.; Dormann, C.; Cornu, G.; Viennois, G.; Bayol, N.; et al. Spatial validation reveals poor predictive performance of large-scale ecological mapping models. *Nat. Commun.* **2020**, *11*, 4540. [CrossRef] [PubMed]
46. Mitchard, E.T.; Feldpausch, T.R.; Brienen, R.J.; Lopez-Gonzalez, G.; Monteagudo, A.; Baker, T.R.; Lewis, S.L.; Lloyd, J.; Quesada, C.A.; Gloor, M.; et al. Markedly divergent estimates of A mazon forest carbon density from ground plots and satellites. *Glob. Ecol. Biogeogr.* **2014**, *23*, 935–946. [CrossRef] [PubMed]
47. Chen, Q.; Laurin, G.V.; Valentini, R. Uncertainty of remotely sensed aboveground biomass over an African tropical forest: Propagating errors from trees to plots to pixels. *Remote Sens. Environ.* **2015**, *160*, 134–143. [CrossRef]
48. McRoberts, R.E.; Westfall, J.A. Effects of uncertainty in model predictions of individual tree volume on large area volume estimates. *For. Sci.* **2014**, *60*, 34–42. [CrossRef]
49. Hyde, P.; Nelson, R.; Kimes, D.; Levine, E. Exploring LiDAR–RaDAR synergy—Predicting aboveground biomass in a southwestern ponderosa pine forest using LiDAR, SAR and InSAR. *Remote Sens. Environ.* **2007**, *106*, 28–38. [CrossRef]
50. Nelson, R.F.; Hyde, P.; Johnson, P.; Emessiene, B.; Imhoff, M.L.; Campbell, R.; Edwards, W. Investigating RaDAR–LiDAR synergy in a North Carolina pine forest. *Remote Sens. Environ.* **2007**, *110*, 98–108. [CrossRef]
51. Meyer, H.; Reudenbach, C.; Wöllauer, S.; Nauss, T. Importance of spatial predictor variable selection in machine learning applications–Moving from data reproduction to spatial prediction. *Ecol. Model.* **2019**, *411*, 108815. [CrossRef]